Research Square

Preprints are preliminary reports that have not undergone peer review.
They should not be considered conclusive, used to inform clinical practice,
or referenced by the media as validated information.

Histone N-terminal tails act as electrostatic clamps to mechanically stabilize nucleosomes

Sotaro Uemura

uemura@bs.s.u-tokyo.ac.jp

The University of Tokyo https://orcid.org/0000-0001-9701-1803

Satoshi Ogihara

The University of Tokyo

Fritz Nagae

Takumi Oishi

Suguru Hatazawa

The University of Tokyo https://orcid.org/0000-0002-5678-4049

Munetaka Akatsu

Tomoya Kujirai

The University of Tokyo https://orcid.org/0000-0001-5547-9598

Ryo Iizuka

The University of Tokyo https://orcid.org/0000-0002-9328-5628

Itaru Yanagi

Shoji Takada

Kyoto University https://orcid.org/0000-0001-5385-7217

Hitoshi Kurumizaka

The University of Tokyo https://orcid.org/0000-0001-7412-3722

Article

Keywords:

Posted Date: March 20th, 2026

DOI: https://doi.org/10.21203/rs.3.rs-9037611/v1

License: This work is licensed under a Creative Commons Attribution 4.0 International License. Read Full License

Additional Declarations: There is **NO** Competing Interest.

Histone N-terminal tails act as electrostatic clamps to mechanically stabilize nucleosomes

Satoshi Ogihara[1], Fritz Nagae[2,#], Takumi Oishi[1,3], Suguru Hatazawa[3], Munetaka Akatsu[1,3], Tomoya Kujirai[3,4], Ryo Iizuka[1], Itaru Yanagi[1], Shoji Takada[2], Hitoshi Kurumizaka[1,3,4] and Sotaro Uemura[1*]

1. **Department of Biological Sciences, Graduate School of Science, The University of Tokyo, Tokyo, Japan**
2. **Department of Biophysics, Graduate School of Science, Kyoto University, Kyoto, Japan**
3. **Institute for Quantitative Biosciences, The University of Tokyo, Tokyo, Japan**
4. **RIKEN Center for Integrative Medical Sciences, Kanagawa, Japan**

#. Current address: Department of Bioscience, Technical University of Munich, Garching, Germany

Contributions

S.T., H.K. and S.U. conceived the study and designed the experiments. R.I., I.Y., S.T., H.K. and S.U. established the measurement equipment, experimental environment, and analysis system. S.O. performed and analysed the experiments. F.N. performed MD simulations. T.O., S.H., M.A., and T.K. provided the samples. S.T., H.K. and S.U. supervised the experiments. T.O., S.H., T.K., R.I., S.T., H.K. and S.U. contributed to the acquisition of financial support for the project leading to this publication. S.O., F.N., H.K. and S.U. interpreted the data and wrote the paper.

* Corresponding author

Correspondence to: Sotaro Uemura

ORCID ID; 0000-0001-9701-1803

Abstract

Chromatin accessibility is dynamically regulated by DNA–histone interaction stability. Although histone variants and post-translational modifications are known to modulate nucleosome stability, the direct mechanical contribution of histone N-terminal tails remains poorly understood. Here, we integrate solid-state nanopore-based single-molecule force spectroscopy with coarse-grained molecular dynamics (MD) simulations to elucidate the mechanical role of histone tails in nucleosomal DNA stabilization. Nanopore measurements comparing canonical, H3 tail-less, and all tail-less nucleosomes reveal that tail removal significantly lowers the voltage threshold for complete DNA unwinding, indicating weakened DNA-histone interactions. The overall unwinding pathway remains largely unchanged, suggesting that histone tails primarily modulate the energetic barrier for DNA unwrapping rather than the unwinding mechanism itself. MD simulations map tail-DNA contact frequencies along superhelical locations, showing that the H3 N-terminal tail preferentially stabilizes DNA near SHL ±6/±7 and the dyad, functioning as an electrostatic clamp that suppresses initial DNA unwrapping under low external force. Together, these results establish histone N-terminal tails as intrinsic mechanical stabilizers that regulate chromatin accessibility by tuning the energy landscape of DNA unwinding, providing a quantitative framework for understanding tail-mediated epigenetic regulation.

Introduction

Chromatin organization is central to the regulation of genome function. At its core, the nucleosome consists of ~146 base pairs of DNA wrapped around a histone octamer containing H2A, H2B, H3, and H4 proteins [1–3]. While this structure provides the basic framework for DNA packaging, its ability to dynamically unwrap and rewrap is what enables the accessibility required for transcription, replication, and repair [4–6]. The mechanical stability of the nucleosome is therefore not static—it is finely tuned by histone variants, post-translational modifications, and the intrinsically disordered histone tails [7–9].

Among these regulators, histone N-terminal tails play particularly crucial roles. They account for almost 30% of the total amino acid residues in the histone octamer yet remain unresolved in most crystal and cryo-electron microscopy structures because of their high flexibility [10-12]. Despite being unstructured, these tails are densely decorated with lysine and arginine residues, forming extensive electrostatic interactions with the negatively charged DNA backbone [6,13,14]. Through this architecture, histone tails mediate diverse enzymatic modifications—including acetylation, methylation, and ubiquitination—that dynamically tune chromatin accessibility [15–18]. Such epigenetic regulation fundamentally relies on modulating the intrinsic mechanical interactions between histone tails and DNA. While acetylation or methylation alters chemical signatures, these modifications essentially function by tuning the physical "clamping" force that tails exert on the nucleosomal DNA[19-21]. Structural and single-molecule studies have shown that histone tails bridge neighboring nucleosomes [22,23] and provide basal mechanical stability near superhelical locations (SHLs) $\pm$ 6 and $\pm$7 [24,25]. Because post-translational modifications ultimately function by modulating the physical interactions between tails and DNA, a quantitative understanding of the intrinsic mechanical contribution of histone tails is a prerequisite for elucidating how individual modifications regulate chromatin accessibility. Yet, this direct mechanical contribution under force has remained poorly quantified.

Our previous work demonstrated that histone variants, such as H2A.B, alter nucleosomal stability by lowering the energy barrier for DNA unwrapping [26], emphasizing how changes in histone core composition modulate the pathway of nucleosome disassembly under applied force. In contrast, the contribution of individual histone tails to mechanical stability remains to be dissected. Among the four core histones, the

H3 N-terminal tail is the longest and most arginine-rich, exhibiting the highest DNA-binding affinity and the longest residence time on the nucleosomal surface. The H3 tail interacts with DNA at both the entry/exit points (SHLs ±6/±7) and near the dyad (SHL 0)—positions that are critical for initiating DNA unwrapping. These features suggest that the H3 tail may serve as a dominant physical stabilizer, yet its specific mechanical contribution has not been experimentally resolved under controlled force conditions. While solid-state nanopore–based force spectroscopy provides a highly sensitive probe for the overall mechanical stability of single nucleosomes, the resolution of ionic current signals is inherently limited, precluding the direct observation of the local, site-specific contributions of individual histone tails. To overcome this limitation and elucidate the molecular basis of tail-mediated stabilization, we integrated nanopore experiments with coarse-grained molecular dynamics (MD) simulations. This combined approach allows us to map experimental voltage-dependent unwinding behavior onto specific tail–DNA interactions at the sub-nanometer scale. By comparing canonical, H3 tail-less, and all tail-less nucleosomes, we show that the absence of histone tails significantly reduces the voltage threshold required for DNA translocation through the nanopore. MD simulations further map the contact frequencies of histone tails along DNA, revealing that the H3 tail anchors DNA at SHLs ±6/±7 and around the dyad, functioning as an electrostatic clamp that resists initial unwrapping.

Together, these experimental and computational approaches allow us to assess the mechanical contribution of histone tails to nucleosome stability and to identify the specific DNA regions stabilized by individual tails. This work extends nanopore-based force spectroscopy to the analysis of tail-mediated regulation of nucleosome stability.

Results

DNA unwinding measurement

Canonical, H3 tail-less, and all tail-less nucleosomes used in this study (Fig. 1a) were reconstituted *in vitro* with the palindromic 601L DNA sequence (see Methods). To ensure that nucleosomes remain intact under the high ionic strength required for nanopore experiments, we first examined nucleosome stability by gel-

shift analysis at different KCl concentrations (Supplementary Fig. S1). Based on these results, we adopted 300 mM KCl as the measurement condition, at which DNA dissociation was minimal or negligible while maintaining sufficient ionic strength for stable nanopore recordings. Under this condition, DNA dissociation was minimal or negligible. Solid-state nanopores with diameters of 3.0‑4.5 nm were fabricated by dielectric breakdown and used to mechanically unwind DNA from the nucleosome (Fig. 1b). When a voltage was applied, nucleosomes were captured at the pore entrance on the *cis* side, and DNA began to peel continuously from the histone core. Only DNA that fully dissociated from histones was able to pass through to the trans side, whereas the intact histone octamer (~11 nm in diameter) cannot pass through the 3.0–4.5 nm nanopore. This configuration ensures that only fully dissociated DNA translocates to the trans side, consistent with previous nanopore studies of nucleosomes [26]. At 300 mV, canonical nucleosomes generated characteristic current-blockage patterns corresponding to the stepwise peeling of DNA from the histone core (Fig. 1c). These signals were absent in chemically crosslinked nucleosomes, confirming that the ionic current fluctuations reflect the mechanical unwinding of DNA from the histone octamer [26].

Nanopore signal analysis

To further characterize the DNA unwinding process, the current blockage amplitude and dwell time of each event were extracted and plotted in two dimensions for canonical and all tail-less nucleosomes under different applied voltages (Fig. 2a). At low voltages (*e.g.*, 100 mV for canonical nucleosomes), the majority of events exhibited relatively short dwell times and smaller blockages. These populations correspond to "failed" unwinding attempts, where the applied force is insufficient to overcome the DNA-histone affinity, causing the DNA to rewrap and return to the cis side. Notably, the removal of histone tails shifted the emergence of long-lived, large-blockage events-representing complete DNA unwinding‒to significantly lower voltages (100 mV for all tail‑less vs. 200 mV for canonical) (Fig. 2a). While long-dwell events can be observed even in canonical nucleosomes at higher voltages, the relative frequency and the

threshold voltage for these events indicate that histone tails impose a substantial barrier to the initiation of DNA peeling. To quantitatively assess this behavior, dwell-time distributions of events with current blockage ratios ≥0.2 were analyzed (Fig. 2b). While a threshold of 0.3 was used in a previous study [26], we set the threshold at ≥0.2 based on the clear separation of the unwinding event population from baseline noise and transient collisions in the 2D scatter plots (Fig. 2a). Only the peak dwell times of the long-dwell-time population associated with complete DNA unwinding were analyzed, and these decreased progressively with increasing voltage (Fig. 2c), consistent with the well-established voltage-dependent acceleration of molecular translocation in nanopore measurements. In contrast, the short-dwell-time events showed no systematic voltage dependence, consistent with transient collisions or failed unwinding attempts that are independent of the applied force magnitude. We next examined the specific contribution of individual histone tails by directly comparing canonical and H3 tail-less nucleosomes (Fig. S2). In H3 tail-less nucleosomes, the complete DNA unwinding population emerged at intermediate voltages (*e.g.*, 200 mV), showing a trend toward facilitated unwinding compared to canonical nucleosomes, although this effect was less pronounced than that observed in all tail-less nucleosomes (Fig. S2). These results show that removal of the H3 tail alone partially facilitates DNA unwinding, and that additional removal of the remaining tails further lowers the threshold voltage.

To confirm that the observed voltage-dependent trends are independent of the nanopore geometry and electric field configuration, we performed additional measurements under reversed electric field polarity, in which DNA translocation was driven in the *trans*-to-*cis* direction (Fig. S3). Under this reversed configuration, the overall trends including the shift of the complete DNA unwinding population to lower voltages upon histone tail removal−were consistent across all three nucleosome constructs (Fig. S3), confirming that the facilitated DNA unwinding observed for tail-less nucleosomes reflects reduced DNA-histone affinity rather than a directional bias in the measurement setup.

Additionally, when nanopore signals from canonical and all tail-less nucleosomes were temporally normalized and overlaid (Fig. S4), no pronounced differences were observed, unlike the marked alterations reported for H2A.B variant nucleosomes [26]. These results indicate that although histone tail deletion

modulates the voltage threshold and frequency of DNA unwinding events, the fundamental unwinding pathway itself remains largely unchanged by the presence or absence of histone tails. Collectively, these findings suggest that histone tails regulate the stability of DNA-histone interactions and thereby tune the mechanical accessibility of nucleosomal DNA, while the core force-induced DNA unwinding pathway probed by nanopore measurements is conserved irrespective of tail deletion. Collectively, these nanopore measurements demonstrate that histone tails regulate the voltage threshold and frequency of DNA unwinding events while the fundamental unwinding pathway is conserved.

Coarse-grained MD simulations

To gain molecular insights into how histone tails contribute to the dynamics of nucleosome unwrapping, we performed coarse-grained MD simulations of nucleosome translocation through a nanopore. The coarse-grained models for the nucleosome and nanopore were constructed as described in Methods [26–28]. At the initial frame of the simulations, we put a nucleosome model in the vicinity of a nanopore and inserted a linker DNA into the pore (Fig. 3a). In the simulations, we applied the electrostatic field potential calculated by COMSOL to drag the nucleosomal DNA into the pore [29].

We first examined the sub-threshold regime. Under the electrostatic field of 50 mV, none of the nucleosomes completely passed through the pore within the simulation timescale (Fig. S5). However, DNA was inserted and stacked into the nanopore in 10% (2/20) of canonical, 20% (4/20) of H3 tail-less, and 35% (7/20) of all tail-less nucleosome trajectories. In the remaining trajectories, the linker DNA rewrapped around the histone octamer and the nucleosome returned to the cis side (Fig. S5). This simulation result provides a direct molecular interpretation of the experimental signals observed at low voltages. In our experiments, short-lived, small-blockage events dominated at 100 mV for canonical nucleosomes. The MD trajectories reveal that these signals correspond to "failed" unwinding attempts, where DNA partially enters the pore but is ultimately pulled back by the histone core due to insufficient electric force (Fig. S5a and b). The decreased frequency of failed attempts upon tail removal in the simulations is qualitatively consistent with the experimentally observed shift toward lower voltage thresholds for complete unwinding.

When an electrostatic field of 100 mV was applied, complete translocation of nucleosomal DNA through the nanopore was observed in 85% (17 out of 20 independent MD trajectories) for the canonical nucleosome, and in 100% (20/20 trajectories) for both the H3 tail-less and all tail-less nucleosomes. Here, the percentages represent the fraction of independent simulation runs in which the DNA fully exited the nanopore within the simulation time window, as quantified by counting successful translocation events across all trajectories (Fig. 3b). The remaining [15% (3/20)] trajectories of simulations using canonical nucleosome showed a failed attempt of nucleosome unwrapping in the same manner as the case of the 50 mV field. As nucleosomal DNA passed through the pore, the DNA was sequentially detached from a histone octamer (Fig. 3a and 3b). The dwell time in steps for canonical, H3 tail-less and all tail-less nucleosomes to pass through a nanopore was $(5.1 \pm 1.3) \times 10^7$, $(4.2 \pm 2.0) \times 10^7$, and $(3.3 \pm 1.1) \times 10^7$ steps. The progressive reduction in dwell time upon tail removal is qualitatively consistent with the voltage-dependent trends observed in the nanopore experiments (Fig. 2c). Together, our simulations qualitatively recapitulated the experimental observation that histone tails inhibit a nucleosome from unwrapping by a nanopore.

To investigate how histone tails inhibit a nucleosome from unwrapping by a nanopore, we performed coarse-grained MD simulations of a nucleosome without a nanopore model and without electrostatic field potential to sample interactions between histone tails and nucleosomal DNA. The N-terminal tails of H3 frequently contacted DNA at SHL(±7) to SHL(±6) and SHL(±2) to SHL(0), while the N-terminal tails of H4, H2A, and H2B contacted with DNA at SHL(±6) to SHL(±1) (Fig. 4a and 4b). The positions where histone tails interact are in line with results of previous studies using all-atomic MD simulations [30,31]. These results show that the H3 N-terminal tails preferentially contact DNA around the dyad and the entry/exit regions, while the other histone tails contact DNA over a broader range of SHL positions.

The territorial distribution of interactions between DNA and histone tails would explain effects of histone tails upon dynamics of nucleosome unwrapping by a nanopore. As shown in Supplementary Fig. S5, failed attempts of nucleosome unwrapping under the 50 mV field were accompanied by DNA rewrapping around a histone octamer. The removal of the H3 N-terminal tail destabilized DNA-histone interactions at the entry-

and exit-side of nucleosome, supporting the decrease of the failed attempts of nucleosome unwrapping under lower electrostatic field potential. Furthermore, in the 100 mV field, detachment of DNA from a histone octamer was temporally stalled at SHL(−5), SHL(−2), and SHL(+3) (Fig. 3b and 4c). The duration time of stalling at SHL(−2) was reduced by removing the H3 N-terminal tail, which interacts with DNA around a dyad (Fig. 4c; Canonical vs H3 tail-less). On the other hand, the duration time of stalling at SHL(−5) and SHL(+3) was reduced by removing the H4, H2A, and H2B N-terminal tails (Fig. 4c; H3 tail-less vs All tail-less), while the effect of omitting the H3 N-terminal tail was miniscule (Fig. 4c; Canonical vs H3 tail-less). Collectively, these findings suggest that the histone N-terminal tails bind to distinct regions of nucleosomal DNA (Fig. 4d) and work as electrostatic clamps to stabilize DNA-histone interactions across the nucleosome.

Discussion

In this study, we combined solid-state nanopore–based force spectroscopy with coarse-grained MD simulations to quantitatively investigate the contribution of histone N-terminal tails to the mechanical stability of nucleosomal DNA. Nanopore measurements demonstrated that, compared with canonical nucleosomes, H3 tail-less and all tail-less nucleosomes exhibited the characteristic population of large-blockage, long-dwell events at substantially lower applied voltages, indicating a reduced mechanical stability of DNA-histone interactions upon tail removal (Fig. 2a, Fig. S2 and S3).

The direct comparison between canonical and H3 tail-less nucleosomes (Fig. S2) is particularly informative, as it isolates the contribution of the H3 N-terminal tail. In H3 tail-less nucleosomes, the event population with high blockage ratios and long dwell times, corresponding to complete DNA unwinding, appeared at lower voltages than in canonical nucleosomes. This result indicates that removal of the H3 tail alone is sufficient to facilitate DNA dissociation from the histone core. These observations are consistent with a model in which the H3 tail acts as a resistance element during the initial stages of DNA peeling, increasing the probability of rewrapping or failed unwinding events when the applied force is insufficient.

In contrast, temporal normalization and overlay of nanopore current traces from canonical and all tail-less

nucleosomes (Fig. S4) revealed no pronounced differences in the overall unwinding profiles. This behavior differs markedly from the substantial pathway alterations observed for H2A.B variant nucleosomes in Nozawa et al [26]. Together, these results suggest that the primary effect of histone tail deletion is to lower the voltage threshold and modulate the frequency of DNA unwinding events, whereas the fundamental unwinding pathway itself remains largely unchanged. This experimental observation is strongly supported by our coarse-grained MD simulations (Fig. 3b, 4c), which show that the sequential base-pair detachment of DNA and the specific stalling positions (e.g., SHL −5, −2, and +3) are largely conserved across all nucleosome constructs. While tails increase the duration of stalling at these positions, they do not alter the fundamental mechanical sequence of unwinding. Thus, while alterations in the histone core—as observed for some histone variants—modify the electrostatic landscape and thereby affect DNA unwinding dynamics, histone tails predominantly regulate the voltage threshold for initiating DNA unwinding, suggesting that they modulate the underlying energetic barrier for this process.

The MD simulations provide a molecular-level interpretation of these experimental findings. In nanopore translocation simulations, low-voltage conditions yielded trajectories in which DNA partially entered the nanopore but ultimately rewrapped and returned to the *cis* side, corresponding to failed unwinding events. The frequency of such failed trajectories decreased upon tail removal (Fig. S5), consistent with the experimental observation that short-lived, small-blockage events dominate at low voltages, whereas complete unwinding events emerge once sufficient force is applied. At higher voltages (*e.g.*, 100 mV equivalent), the probability of successful translocation increased and the residence time within the pore decreased for tail-less nucleosomes, consistent with the voltage-dependent reduction in dwell time observed experimentally (Fig. 2c).

Analysis of tail–DNA contact probabilities obtained from simulations performed in the absence of a nanopore further clarifies how histone tails stabilize nucleosomal DNA (Fig. 4a and 4b). The H3 N-terminal tail preferentially interacts with DNA around SHL(±7)–(±6) and SHL(±2)–0, consistent with previous all-atom MD simulations [30,31] and structural studies showing that the H3 tail stabilizes DNA near the entry/exit regions [24,25], whereas the H4/H2A/H2B tails display broader interactions spanning SHL(±6)–

(±1). This spatial segregation of tail–DNA contacts provides a structural basis for the observed differences in pore-stacking behavior and dwell times at specific unwrapping states (Fig. 4c and 4d). In this framework, the H3 tail contributes primarily to stabilizing DNA near the dyad and at SHL(±6)–(±7), while the H4/H2A/H2B tails show broader contacts spanning SHL(±6)–(±1). Although these contact regions partially overlap around SHL(±6), the two groups of tails exhibit complementary spatial distributions that collectively increase the resistance of the nucleosome to mechanical unwinding.

These findings have direct implications for understanding the physical basis of chromatin accessibility regulation by histone tails. Histone tails are enriched in positively charged residues and interact electrostatically with DNA; post-translational modifications such as acetylation weaken these interactions and promote DNA exposure [19–21]. By probing force-induced DNA unwinding at the single-molecule level, our results show that tail removal lowers the voltage threshold for initiating DNA peeling without fundamentally altering the unwinding pathway. This supports a model in which histone tails function as electrostatic clamps that suppress the probability of initial DNA unwrapping, thereby tuning chromatin accessibility through modulation of the energy barrier rather than the reaction pathway itself.

The present study establishes a framework for dissecting the mechanical contributions of histone tails, and several extensions merit consideration. Future studies employing chemically or enzymatically modified histones—such as site-specifically acetylated or methylated variants—will enable a more direct connection between specific modifications and the mechanical stabilization at individual SHL positions. Similarly, adapting nanopore conditions to lower ionic strengths, potentially through the use of smaller or modified nanopores, would bring the measurements closer to physiological relevance. Extending this approach to higher-order chromatin structures, such as nucleosome arrays or complexes with linker histones and DNA-binding proteins, will further enable quantitative dissection of how local tail-mediated stabilization propagates to genome-scale regulation of chromatin mechanics.

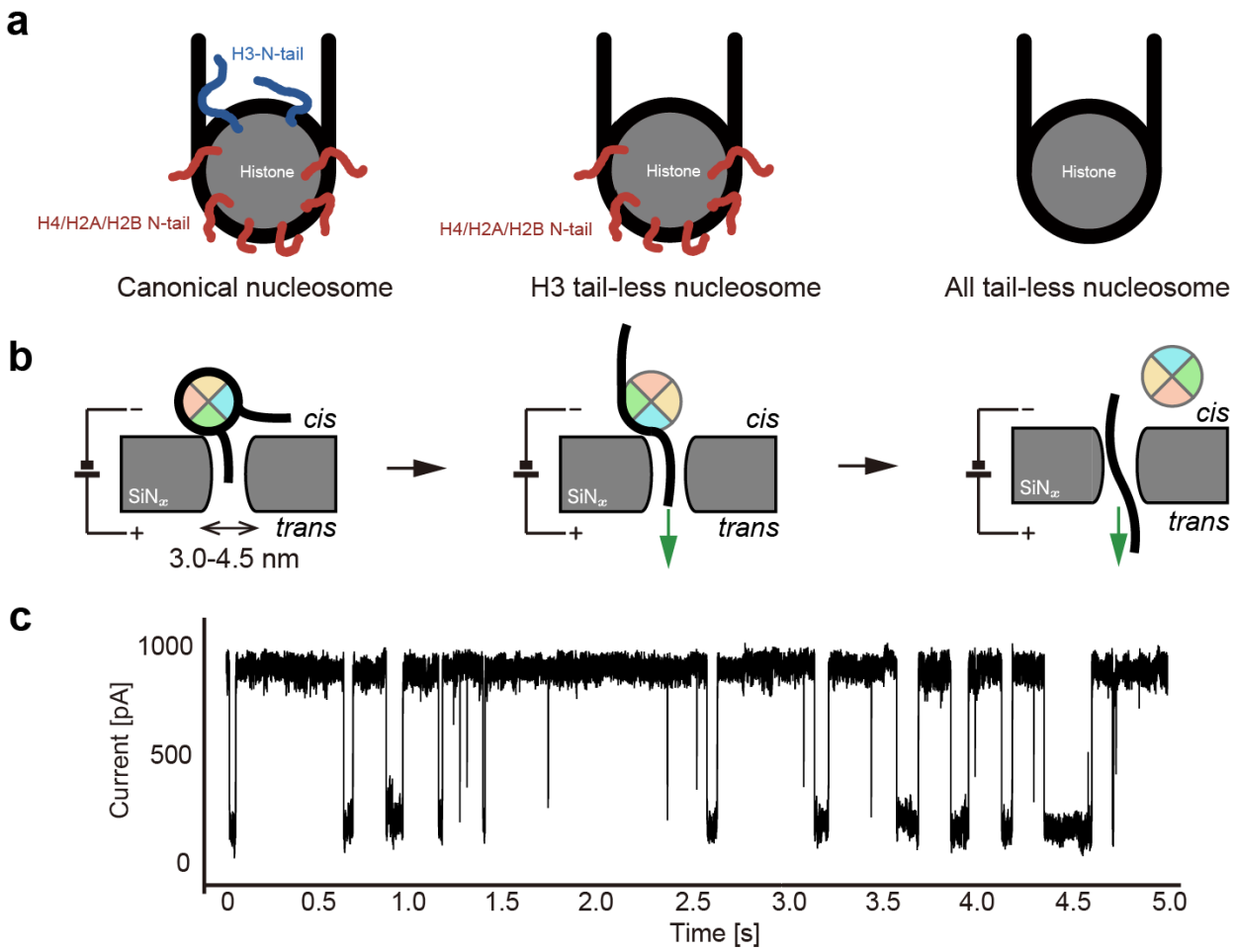


Fig. 1: Schematic representation of nucleosomes with histone tail deletions and the nanopore measurement setup.

a. Schematic illustrations of the three nucleosome constructs used in this study: canonical nucleosome with intact histone tails (left), H3 tail–less nucleosome (middle), and all tail–less nucleosome (right). Blue lines represent the N-terminal tails of H3, and red lines represent the N-terminal tails of H2A, H2B, and H4. **b.** Schematic of the solid-state nanopore measurement used to probe DNA–histone interactions. A nucleosome is captured at the nanopore entrance from the *cis* chamber (left). Upon application of an external electric field, DNA begins to peel from the histone core, undergoing progressive unwinding (middle). After complete dissociation of DNA from histones, only free DNA strands translocate through the nanopore to the trans side (right). **c.** Representative nanopore current trace obtained from a canonical nucleosome at 300 mV over a 5-s interval.

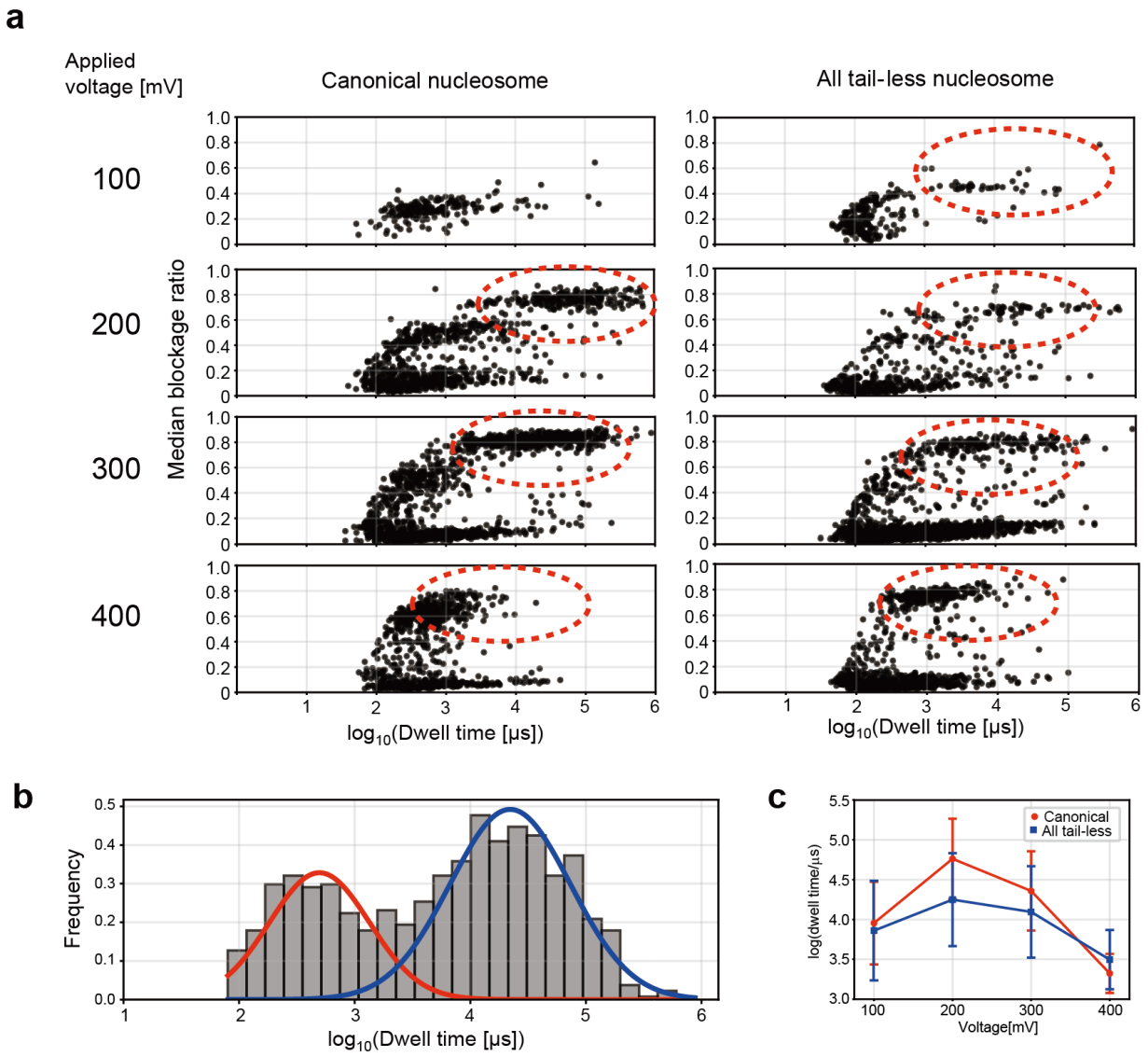


Fig. 2: Scatter plots and Gaussian fitting analysis of nanopore signals from canonical and all-tail–less nucleosomes.

a. Scatter plots of current blockage ratio ($\Delta I/I_0$) versus dwell time for canonical nucleosomes (left) and all tail–less nucleosomes (right) under different applied voltages. Red dot circles indicate the appearance of these new event populations at 200 mV for canonical nucleosomes and 100 mV for all tail–less nucleosomes. **b.** The histograms of dwell time for events with deep blockade ≥0.2 and their fitting with double Gaussian distributions (red and blue curves). Shown here is the fitting result for canonical nucleosomes at 300 mV **c**. Average duration time of events with deep blockage and long duration time as a function of the voltage. Error bars represent the standard deviation.

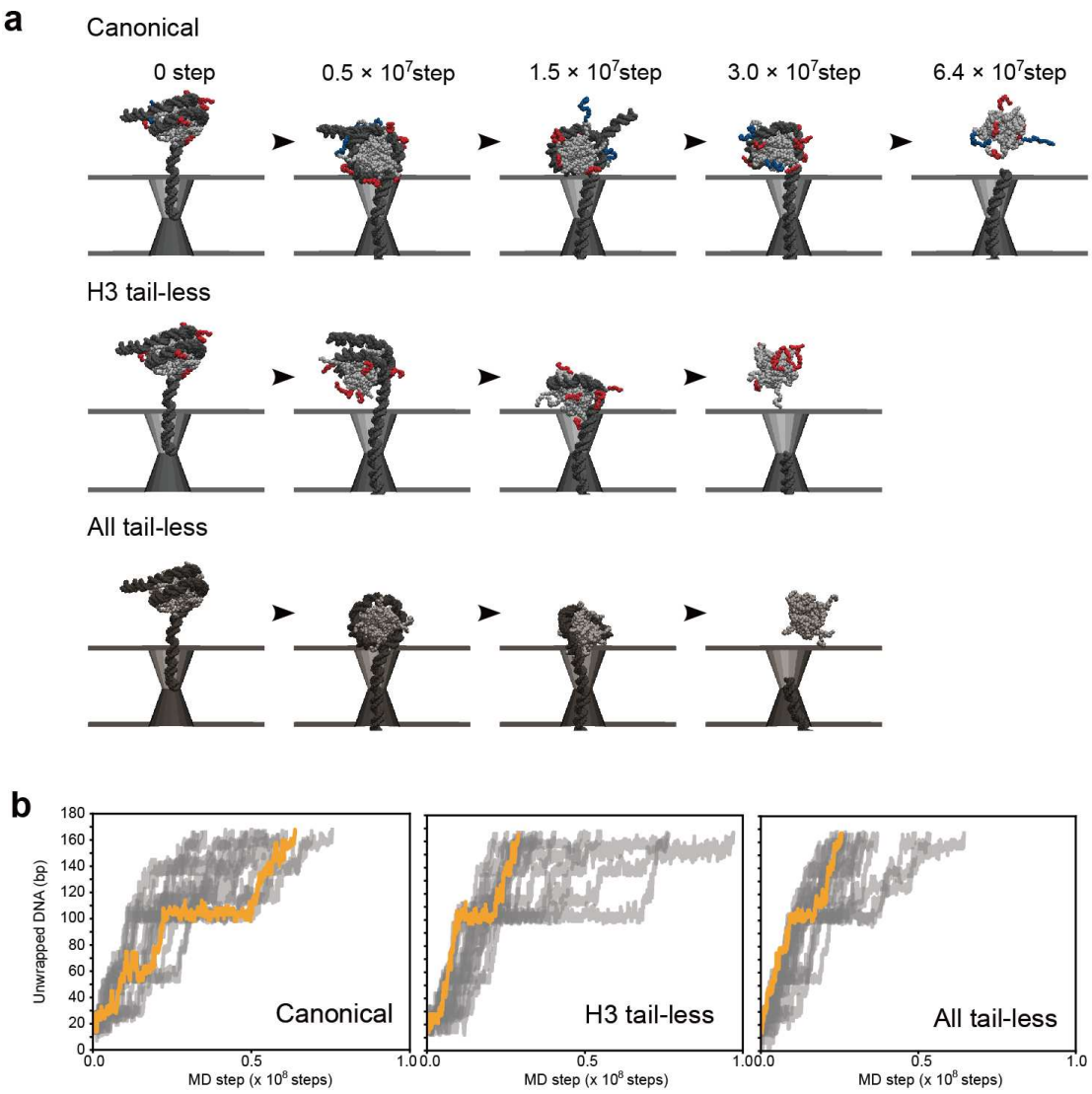


Fig. 3: Coarse-grained molecular dynamics simulations of nucleosome passage through a nanopore.

a Representative snapshots from coarse-grained MD simulation trajectories showing the nanopore translocation process for canonical nucleosomes (top), H3 tail–less nucleosomes (middle), and all tail–less nucleosomes (bottom) under an applied voltage of 100 mV. Blue, red, black, and gray beads represent the N-terminal tails of H3, the N-terminal tails of H2A/H2B/H4, DNA, and histones, respectively. The silver object represents solid-state nanopore, which is cut in half for visualization. **b** Time courses of nucleosomal DNA unwrapping for the three nucleosome constructs at 100 mV. For each condition (canonical, H3 tail–less, and all tail–less), the extent of DNA unwrapped from the histone core (bp) is plotted as a function of MD simulation steps. All trajectories that successfully passed through the nanopore are overlaid, with one representative trajectory highlighted in orange, and all others shown in gray.

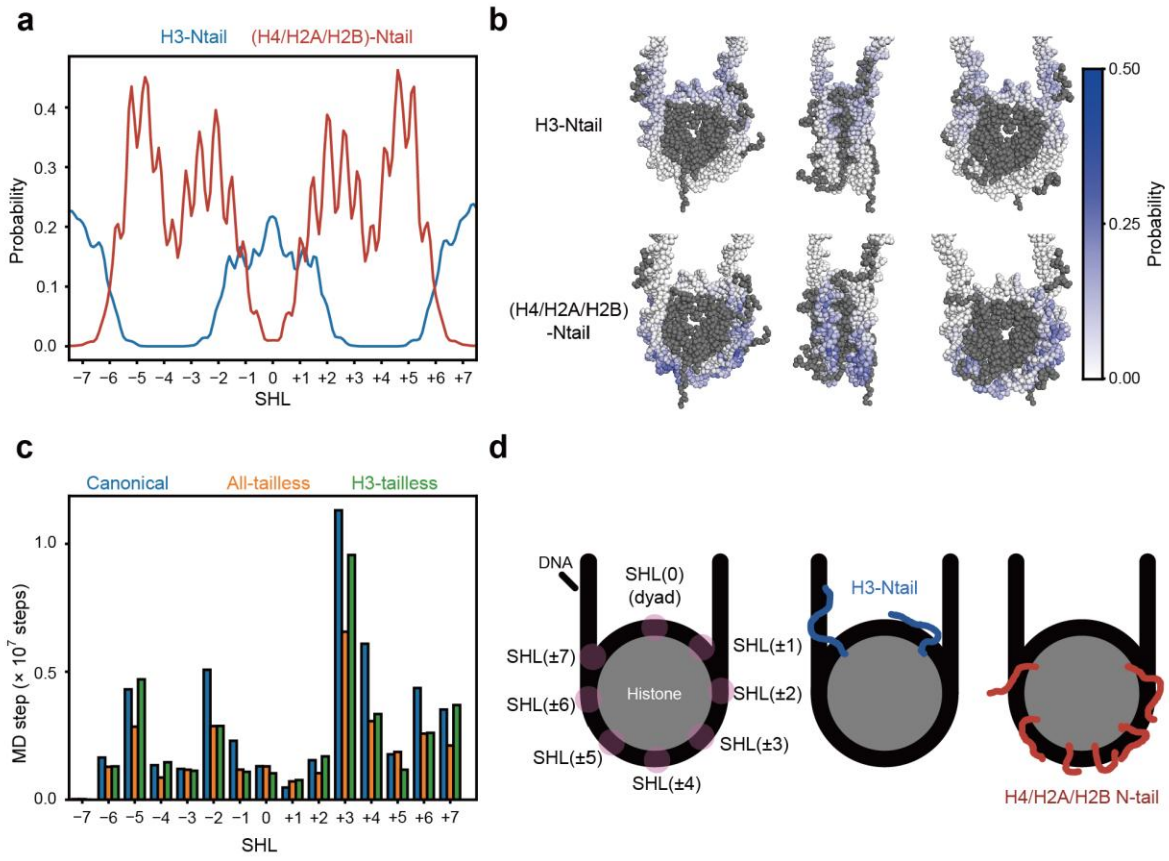


Fig. 4: Histone tail–DNA contact analysis and tail-mediated stabilization during nanopore translocation. **a** Probability of histone tail–DNA contacts along the nucleosomal DNA obtained from coarse-grained MD simulations. Contact probabilities were calculated for the H3 N-terminal tail (blue) and the combined H4/H2A/H2B N-terminal tails (red). The horizontal axis represents DNA positions converted from base-pair indices to superhelical location (SHL). **b** Mapping of the histone tail–DNA contact probabilities onto the coarse-grained nucleosome structure. Contact frequency is color-coded, with more intense blue indicating stronger or more frequent contacts between histone tails and DNA. Gray beads represent histones. **c** Bar plots of the pore-stacking duration time during nanopore translocation at 100 mV as a function of the DNA unwrapped state, expressed in SHL units. Results are shown for canonical (blue), H3 tail-less (green), and all tail-less nucleosomes (orange). d Schematic summary illustrating the major binding regions of H3 N-terminal tails (blue) and H4/H2A/H2B N-terminal tails (red) along the DNA superhelical locations.

Supplementary Movie 1: The representative trajectories in which a canonical nucleosome passed through a nanopore at 100 mV voltage. Blue, red, black, and gray beads represent the N-terminal tails of H3, the N-terminal tails of H2A/H2B/H4, DNA, and histones, respectively. The silver object represents solid-state nanopore, which is cut in half for visualization.

Supplementary Movie 2: The representative trajectories in which an H3 tail-less nucleosome passed through a nanopore at 100 mV voltage. The color scheme is the same as Supplementary Movie 1.

Supplementary Movie 3: The representative trajectories in which an all tail-less nucleosome passed through a nanopore at 100 mV voltage. The color scheme is the same as Supplementary Movie 1.

Methods

Preparation of the histones

Human histones H2A, H2B, H3.1, and H4, as well as their tailless variants (tlH2A, tlH2B, tlH3, and tlH4) were purified according to the methods described previously 12,32,33. The tailless mutants were designed based on trypsin-sensitive regions and crystal structure of the nucleosome 2,34. Briefly, full-length and tailless human histones (tlH2A (a.a. 10–129), tlH2B (a.a. 25–125), tlH3 (a.a. 28–135), and tlH4 (a.a. 16–102)) were expressed in Escherichia coli as N-terminally 6×histidine-tagged proteins. After the sonication and centrifugation of the harvested cells, the insoluble fractions were purified by Ni-NTA affinity chromatography (Qiagen) under denaturing conditions. The histone proteins were subsequently cleaved from the histidine-tag using thrombin protease and further purified by Mono S cation-exchange chromatography (Cytiva). Purified histones were dialyzed against 2 mM β-mercaptoethanol, lyophilized, and stored as dry powder at 4°C.

Preparation of DNA fragments

The 193 base-pair (bp) palindromic Widom 601L DNA fragment was prepared as described previously [3,26,35]. In brief, the DNA sequence was excised from a pGEM-T Easy vector (Promega) containing multiple repeats of the 601L half-sequence by digestion with EcoRV (Takara Bio). The excised fragments were purified by PEG precipitation, dephosphorylated using calf intestinal alkaline phosphatase (Takara Bio), and extracted with phenol–chloroform. Following ethanol precipitation, the DNA fragments were digested with HinfI (Takara Bio) and purified by TSK-DEAE ion-exchange chromatography (Tosoh). The purified fragments were ligated to form the full-length 193 bp DNA, which was subsequently separated using a Prep Cell apparatus (Bio-Rad). The final DNA fragments were concentrated and stored at −25°C. The sequence of the 193 bp Widom 601L DNA is as follows: 5′-ATCACGTAATATTGGCCAGCTAGGATCACAATCCCGGTGCCGAGGCCGCTCAATTGGTCGTAG

ACAGCTCTAGCACCGCTTAAACGCACGTACGGAATCCGTACGTGCGTTTAAGCGGTGCTAGAG
CTGTCTACGACCAATTGAGCGGCCTCGGCACCGGGATTGTGATCCTAGCTGGCCAATATTACG
TGAT-3′.

Reconstitution and purification of nucleosomes

Histone octamers were prepared as previously described [32]. Equimolar amounts of each histone were mixed under denaturing conditions and refolded by stepwise dialysis into non-denaturing buffer. The resulting histone octamers were purified by size-exclusion chromatography using a HiLoad 16/60 Superdex 200 column (Cytiva), concentrated, and stored at −80°C. Nucleosomes were reconstituted by salt dialysis using the purified histone octamers and 601L DNA. In this study, we prepared three types of nucleosomes: the canonical nucleosome (containing full-length H2A, H2B, H3, and H4), the all tail-less nucleosome (containing tlH2A, tlH2B, tlH3, and tlH4), and the H3 tail-less nucleosome (containing tlH3 and full-length H2A, H2B, and H4). The reconstituted nucleosomes were purified using a Prep Cell apparatus (Bio-Rad) and dialyzed against a buffer containing 20 mM Tris–HCl (pH 7.5), 1 mM DTT, and 5% glycerol, concentrated, and stored at −80°C.

Salt stability assessment of the nucleosome

Nucleosomes were incubated at 30°C for 30 minutes in a buffer containing 20 mM HEPES–KOH (pH 7.5), 1mM DTT, 5% glycerol, 100 nM nucleosome with potassium chloride concentratioins of 0, 100, 200, 300, 400, or 500 mM. The resulting nucleosomes were analyzed by non-denaturing PAGE.

Nanopore fabrication and measurement

To ensure accurate baseline measurement, rare events exhibiting current increases were excluded during the initial detection, as they were likely attributable to instrumental noise or external interference. Therefore, only events showing a decrease in current were included in this analysis. Ionic current events were then initially detected from the recorded waveforms using Nanolyzer (Northern Nanopore Instruments) and EWMAuto [36,37]. While these standard tools provided robust initial event detection, the

complex waveform characteristics required further refinement for precise dwell time extraction. We therefore applied a dynamic boundary re-definition algorithm to these detected events. For each event, the current trace after baseline correction was analyzed to identify candidate regions where the current temporarily dropped below a threshold of -30 pA. This step served solely to localize the event center for the subsequent boundary search, as rigorous thresholding had already been performed during the initial detection. The global minimum (i.e., the lowest current value) within these candidate regions was designated as the event center. To determine the true event boundaries, a bidirectional search was performed along the time axis starting from this center point. The start point was defined as the last instant preceding the center where the current recovered to the baseline (0 pA), and the end point was defined as the first instant succeeding the center where the current recovered to the baseline. Events that failed to return to the baseline at either boundary, or those yielding a non-positive duration after redefinition, were excluded from further analysis. For events satisfying the redefinition criteria, blockage ratios were calculated using the current values within the redefined intervals. To mitigate the impact of outliers, the median current value was used to calculate the median blockage ratio. We confirmed that there were no significant differences in the event distributions in the 2D scatter plots when comparing the median blockage ratio and the average blockage ratio. The final number of analyzed events for canonical nucleosomes was 204 at 100 mV, 937 at 200 mV, 1476 at 300 mV, and 748 at 400 mV. For all tail-less nucleosomes, the number of events was 229 at 100 mV, 545 at 200 mV, 1626 at 300 mV, and 933 at 400 mV. These variations in event numbers reflect an increase in capture rate driven by voltage across approximately consistent recording durations for each sample. The number of events analyzed for the supplementary data is detailed in the respective figure legends in the Supplementary Information.

Coarse-grained nucleosome models

We employed the AICG2+ model which represents one amino acid as one single bead located on a position of the Cα atom and the 3SPN.2C which represents one nucleotide as three beads located on center-of-masses of phosphate, sugar, and base groups [27,28]. To stabilize a reference structure of a histone octamer

(PDB ID: 1KX5), we applied structure-based potentials 10. Also, strength of the potentials between an H3/H4 tetramer and H2A/H2B dimers was scaled by a factor of 0.3 as previously developed [38], which successfully reproduced the experimentally suggested metastable state in nucleosome assembly process. To describe dynamics of intrinsically disordered region, we applied statistical local potentials which were derived from the statistical analysis of loop regions in the protein data bank structures [39]. For DNA, structure-based potential was applied to stabilize the B-form structure and to reproduce sequence-dependent curvature of double-stranded DNA [28]. Between DNA and histones, electrostatic, excluded volume, and hydrogen-bonding interactions were applied to reproduce a reference structure of a nucleosome and a salt-dependent disassembly process of a nucleosome [4,40,41]. The electrostatic potentials were modelled based on the Debye-Hückel's theory to treat the effects of ions implicitly. To optimize partial charges on protein beads of histone globular regions, we employed the RESPAC algorithm to reproduce the surface electrostatic potentials in the all-atomic structure of a histone octamer [42]. For histone tails, we used integer charges (±1) on lysine, arginine, aspartic acid, and glutamic acid. We set −0.6e and −1e to the DNA phosphate bead for intra-DNA and protein-DNA interactions, respectively. The settings of phosphate charge accounts for the counter ion condensation around the phosphate groups and release of counter ion upon DNA-protein complex formation.

The initial structure of a canonical nucleosome was prepared based on coordinates in the crystal structure (PDB ID: 1KX5) [10]. The initial conformations of the flexible histone tails were determined using MODELLER [43]. We exchanged the DNA sequence in the structures into the Widom 601L DNA sequence, and 23 bp double-stranded DNA segments were connected to both linkers of the nucleosome, generating the 193 bp of DNA substrate. The initial structures of all-tail less and H3-tail less nucleosomes were prepared by omitting the N-terminal tails of H3 (residue 1 to 27), H4 (residue 1 to 15), H2A (1 to 9), and H2B (1 to 24) from a canonical nucleosome.

Nanopore simulation model

$$V_{pore}(r_i) = V_{pulse}(z_i)V_{torus}(r_i) \quad (1)$$

We have previously developed a nanopore model based on the torus-shaped excluded volume potential, and given as

$$V_{torus}(r_i) = \begin{cases} 0, (d_i(r_i) > r^u) \\ 4\varepsilon\left[\left(\frac{\sigma}{d_i(r_i)}\right)^{12} - \left(\frac{\sigma}{r^u}\right)^{12}\right], (r^l < d_i(r_i) \le r^u) \\ 4\varepsilon\left[\left(\frac{\sigma}{r^l}\right)^{12}\left\{1 + 12\left(\frac{r^l - d_i(r_i)}{r^l}\right)\right\} - \left(\frac{\sigma}{r^u}\right)^{12}\right], (d_i(r_i) \le r^l) \end{cases} \quad (2)$$

$$d_i(r_i) = \|r_i(x, r, \theta) - r_i(0, M, \theta)\| - m \quad (3)$$

$$m = \frac{L^2 + (w_u - w_l)^2}{4(w_u - w_l)} \quad (4)$$

$$M = m + \frac{w_l}{2} \quad (5)$$

$$V_{pulse}(z_i) = \begin{cases} \frac{1}{2}\left[1 + tanh\left(z_i + \frac{L}{2}\right)\right], & z_i < 0 \\ \frac{1}{2}\left[1 - tanh\left(z_i - \frac{L}{2}\right)\right], & z_i \ge 0 \end{cases} \quad (6)$$

where ri and zi is the position of the i-th particle in cylindrical coordinate and its z-component [26]. The parameters ru = 3.0σ and rl = 0.8σ are the upper and lower boundaries of the potential energy. We set the parameter of the entrance diameter wu, the minimum diameter wl, and the thickness of a nanopore L to 1.0, 80, 32, and 132 Å, respectively. The parameters for excluded volume potential ε and σ were set to 1.0 kcal/mol and 1.0 Å.

In the simulations of a nucleosome passing through a nanopore, we applied local electrostatic forces to DNA and protein beads according to the electric field computed by the COMSOL Multiphysics software [29]. We used the B-spline function to interpolate the field of 2 Å grid resolution. The electrostatic forces applying to the DNA phosphate group were scaled by 0.25 to account for counterion condensation around dsDNA.

Molecular dynamics simulation

We performed all the simulations using the software CafeMol 3.2.1 [44]. We used the Langevin dynamics to integrate the equations of motion with a timestep of 0.3 CafeMol time unit. The temperature, friction coefficient, and the monovalent ion concentration were set to 300 K, 0.843, and 300 mM, respectively. Because the dielectric constant of the solvent was dependent on temperature and ionic strength, we set to $\varepsilon = 72.2$, computed using an empirical formula derived by Stogryn [45]. We computed all the simulations of nucleosome unwrapping for 1×10^8 steps and saved the trajectories every 10^4 steps. It should be noted that the absolute voltage values in our coarse-grained MD simulations (50 and 100 mV) differ from the experimental values (100–400 mV). Such discrepancies are commonly observed in nanopore simulations and arise primarily from the simplification of electrostatic interactions, including the scaling of phosphate charges (0.25×) to account for counterion condensation. Despite the difference in absolute magnitude, the simulations qualitatively and phenomenologically recapitulate the experimental observations. Specifically, the 50 mV MD field corresponds to the sub-threshold regime where DNA rewrapping (failed attempts) dominates, while the 100 mV field reflects the regime where sufficient electric force overcomes the energetic barrier imposed by histone tails to achieve complete translocation.

Statistics and Reproducibility

Nanopores were fabricated on commercially available 12 nm-thick silicon chips (NXDB-50B405A122; Norcada) following the protocols provided by Northern Nanopore Instruments. The diameters of the fabricated nanopores ranged from 3.0 to 4.5 nm. For single-molecule detection, ionic currents were recorded using an Axopatch 200B amplifier (Molecular Devices). Data were acquired at a sampling rate of 250 kHz and filtered at 10 kHz using the built-in low-pass filter. Although the low-pass filter generally requires consideration for events with durations of 100–200 μs due to signal attenuation, the occurrence of such short-lived events was negligible in the dataset analyzed in this study; therefore, the filter effects were

not accounted for in the current analysis. The recording buffer for nucleosome measurements consisted of 300 mM KCl and 10 mM HEPES-KOH (pH 7.0). The final concentration of all nucleosome samples (canonical, all tail-less) was adjusted to 2 nM for the nanopore measurements, unless otherwise specified.

The use of large language models

ChatGPT and Claude, large language model developed by OpenAI and Anthropic respectively, were used in a strictly auxiliary role to support the writing process. This included assistance with phrasing and grammar correction. The author remains fully responsible for the content and conclusions of the manuscript.

References

1. Kornberg, R. D. Chromatin structure: a repeating unit of histones and DNA. *Science* **184**, 868–71 (1974).
2. Luger, K., Mäder, A. W., Richmond, R. K., Sargent, D. F. & Richmond, T. J. Crystal structure of the nucleosome core particle at 2.8 A resolution. *Nature* **389**, 251–60 (1997).
3. Bednar, J. et al. Structure and dynamics of a 197 bp nucleosome in complex with linker histone H1. *Mol. Cell* **66**, 384–397.e8 (2017).
4. Li, G. & Widom, J. Nucleosomes facilitate their own invasion. *Nat. Struct. Mol. Biol*. **11**, 763–769 (2004).
5. Clapier, C. R. & Cairns, B. R. The biology of chromatin remodeling complexes. *Annu. Rev. Biochem*. **78**, 273–304 (2009).
6. Zhou, K., Gaullier, G. & Luger, K. Nucleosome structure and dynamics are coming of age. *Nat. Struct. Mol. Biol*. **26**, 3–13 (2019).
7. Tachiwana, H. et al. Structural basis of instability of the nucleosome containing a testis-specific histone variant, human H3T. *Proc. Natl Acad. Sci. USA* **107**, 10454–10459 (2010).
8. Arimura, Y. *et al.* Structural basis of a nucleosome containing histone H2A.B/H2A.Bbd that transiently associates with reorganized chromatin. *Sci Rep* **3**, 3510 (2013).
9. Talbert, P. B. & Henikoff, S. Histone variants on the move: substrates for chromatin dynamics. *Nat. Rev. Mol. Cell Biol*. **18**, 115–126 (2017).
10. Davey, C. A., Sargent, D. F., Luger, K., Maeder, A. W. & Richmond, T. J. Solvent mediated interactions in the structure of the nucleosome core particle at 1.9 Å resolution. *J. Mol. Biol*. **319**, 1097–1113 (2002).
11. McGinty, R. K. & Tan, S. Nucleosome structure and function. *Chem. Rev*. **115**, 2255–2273 (2015).
12. Oishi, T. et al. Contributions of histone tail clipping and acetylation in nucleosome transcription by RNA polymerase II. *Nucleic Acids Res*. **51**, 10364–10374 (2023).
13. Zheng, C. et al. Structures and interactions of the core histone tail domains. *Biopolymers* **68**, 539–546 (2003).
14. Hansen, J. C. Conformational dynamics of the chromatin fiber in solution: determinants, mechanisms, and functions. *Annu. Rev. Biophys. Biomol. Struct.* **31**, 361–392 (2002).
15. Bannister, A. J. & Kouzarides, T. Regulation of chromatin by histone modifications. *Cell Res*. **21**, 381–395 (2011).
16. Jenuwein, T. & Allis, C. D. Translating the histone code. *Science* **293**, 1074–1080 (2001).
17. Zentner, G. E. & Henikoff, S. Regulation of nucleosome dynamics by histone modifications. *Nat. Struct. Mol. Biol*. **20**, 259–266 (2013).
18. Tessarz, P. & Kouzarides, T. Histone core modifications regulating nucleosome structure and dynamics. *Nat. Rev. Mol. Cell Biol*. **15**, 703–708 (2014).
19. Lee, D. Y., Hayes, J. J., Pruss, D. & Wolffe, A. P. A positive role for histone acetylation in transcription factor access to nucleosomal DNA. *Cell* **72**, 73–84 (1993).
20. Vettese-Dadey, M. et al. Acetylation of histone H4 plays a primary role in enhancing transcription factor binding to nucleosomal DNA in vitro. *EMBO J.* **15**, 2508–2518 (1996).
21. Kouzarides, T. Chromatin modifications and their function. *Cell* **128**, 693–705 (2007).
22. Schalch, T., Duda, S., Sargent, D. F. & Richmond, T. J. X-ray structure of a tetranucleosome and its implications for the chromatin fibre. *Nature* **436**, 138–141 (2005).
23. Dorigo, B. et al. Nucleosome arrays reveal the two-start organization of the chromatin fiber. *Science* **306**, 1571–1573 (2004).
24. Li, G. et al. Rapid spontaneous accessibility of nucleosomal DNA. *Nat. Struct. Mol. Biol*. **12**, 46–53 (2005).
25. Bilokapic, S. et al. Histone octamer rearranges to adapt to DNA unwrapping. *Nat. Struct. Mol. Biol*. **25**, 101–108 (2018).
26. Nozawa, H. *et al*. Nucleosomal DNA unwinding pathway through canonical and non-canonical

histone disassembly. *Commun. Biol*. **7**, 1144 (2024).
27. Li, W. et al. Energy landscape views for interplays among folding, binding, and allostery of calmodulin domains. *Proc. Natl. Acad. Sci. USA* **111**, 10550–10555 (2014).
28. Freeman, G. S. et al. Coarse-grained modeling of DNA curvature. *J. Chem. Phys*. **141**, 165103 (2014).
29. Choudhary, A. et al. Multi-resolution simulation of DNA transport through large synthetic nanostructures. *Phys. Chem. Chem. Phys*. **24**, 2706–2716 (2022).
30. Peng, Y. et al. Binding of regulatory proteins to nucleosomes is modulated by dynamic histone tails. *Nat. Commun*. **12**, 5280 (2021).
31. Armeev, G. A. et al. Histone dynamics mediate DNA unwrapping and sliding in nucleosomes. *Nat. Commun*. **12**, 2387 (2021).
32. Kujirai, T. et al. Methods for preparing nucleosomes containing histone variants. *Methods Mol. Biol*. **1832**, 3–20 (2018).
33. Iwasaki, W. et al. Contribution of histone N-terminal tails to the structure and stability of nucleosomes. *FEBS Open Bio* **3**, 363–369 (2013).
34. Böhm, L. et al. Proteases as structural probes for chromatin: the domain structure of histones. *Biosci. Rep.* **4**, 365-386 (1984).
35. Chua, E. Y. D. et al. The mechanics behind DNA sequence-dependent properties of the nucleosome. *Nucleic Acids Res*. **40**, 6338–6352 (2012).
36. Waugh, M. et al. Solid-state nanopore fabrication by automated controlled breakdown. *Nat. Protoc.* **15**, 122–143 (2020).
37. Akita, R. et al. Voltage-matrix nanopore profiling for the discrimination of protein mixtures. *Chem. Sci.* **16**, 18607–18615 (2025).
38. Brandani, G. B. et al. The kinetic landscape of nucleosome assembly: A coarse-grained molecular dynamics study. *PLoS Comput. Biol*. **17**, e1009253 (2021).
39. Terakawa, T. et al. Multiscale ensemble modeling of intrinsically disordered proteins: p53 N-terminal domain. *Biophys. J.* **101**, 1450–1458 (2011).
40. Niina, T. et al. Sequence-dependent nucleosome sliding in rotation-coupled and uncoupled modes revealed by molecular simulations. *PLoS Comput. Biol*. **13**, e1005880 (2017).
41. Kenzaki, H. & Takada, S. Partial unwrapping and histone tail dynamics in nucleosome revealed by coarse-grained molecular simulations. *PLoS Comput. Biol.* **11**, e1004443 (2015).
42. Terakawa, T. et al. RESPAC: Method to determine partial charges in coarse-grained protein model and its application to DNA-binding proteins. *J. Chem. Theory Comput*. **10**, 711–721 (2014).
43. Fiser, A. et al. Modeller: generation and refinement of homology-based protein structure models. *Methods Enzymol*. **374**, 461–491 (2003).
44. Kenzaki, H. et al. CafeMol: A coarse-grained biomolecular simulator for simulating proteins at work. *J. Chem. Theory Comput*. **7**, 1979–1989 (2011).
45. Stogryn, A. Equations for calculating the dielectric constant of saline water. *IEEE Trans. Microw. Theory Techn.* **19**, 733–736 (1971).

Acknowledgements

The authors would like to thank Dr. Keiko Esashika (Keio University, Japan) and Mr. Utaro Nakamura for supporting experimental setup and developing signal extraction algorithm, respectively. This work was supported by JST, CREST (Grant no. JPMJCR2231, Grant no. JPMJCR24T3), ERATO (Grant no. JPMJER1901, Grant no. JPMJER2002), SPRING (Grant no. JPMJSP2108), PRESTO (Grant no. JPMJPR25N9), JSPS (Grant no. JP23H05475, Grant no. JP24H02328, Grant no. JP25KJ1033, Grant no. JP23K17392, Grant no. JP24H02319, Grant no. JP24H00062, Grant no. 20J00261), and Research Support Project for Life Science and Drug Discovery (Basis for Supporting Innovative Drug Discovery and Life Science Research (BINDS)) from AMED (Grant no. JP25ama121009).

Ethics declarations

No competing interests

Data Availability Statement

The custom Python application developed for offline nanopore data analysis is available under the MIT license. The source code is hosted on GitHub at https://github.com/Satoshi-Ogi/Nucleosome_Paper_2026, and the specific version used in this study is permanently archived in Zenodo at https://doi.org/10.5281/zenodo.18822312.

Supplementary Files

This is a list of supplementary files associated with this preprint. Click to download.

- canonicalnanoporepassing.mp4
- h3taillessnanoporepassing.mp4
- alltaillessnanoporepassing.mp4
- OgiharaetalSupplementaryInformationsubmission.pdf